Enabling Solution Processible COFs through Suppression of Precipitation during Solvothermal Synthesis

Safiya Khalil[†], Matthew D. Meyer[‡], Abdullah Alazmi[†], Mohammad H. K. Samani[†], Po-Chun Huang[†], Morgan G. Barnes[^], Amanda B. Marciel[†] an and Rafael Verduzco[*,†,§,^]

†Department of Chemical and Biomolecular Engineering, Rice University, 6100 Main Street, MS-362, Houston, Texas 77005, United States

‡Shared Equipment Authority, Rice University, 6100 Main Street, Houston, Texas 77005, United States

§ Nanosystems Engineering Research Center for Nanotechnology-Enabled Water Treatment Rice University, 6100 Main Street, Houston, TX, 77005, USA

^Department of Materials Science and NanoEngineering, Rice University, 6100 Main Street, MS-364, Houston, Texas 77005, United States

ABSTRACT. Covalent organic frameworks (COFs) are crystalline, nanoporous materials of interest for various applications. However, current COF synthetic routes lead to insoluble aggregates which hamper processing and prohibit their use in many applications. Here, we report a novel COF synthesis method that produces a stable, homogeneous suspension of crystalline COF nanoparticles. Our approach involves the use of a polar solvent, di-acid catalyst, and slow reagent mixing procedure at elevated temperatures which all together enable access to crystalline COF nanoparticle suspension that does not aggregate or precipitate when kept at elevated temperatures. On cooling, the suspension undergoes a thermoreversible gelation transition to produce crystalline and highly porous COF materials. We demonstrate that this method enables the preparation of COF monoliths, membranes, and films using conventional solution processing techniques. We show that the modified synthesis approach is compatible with various COF chemistries, including both large- and small-pore imine COFs, hydrazone-linked COFs, and COFs with rhombic and hexagonal topology, and in each case, we demonstrate that the final product has excellent crystallinity and porosity. The final materials contain both micro- and macropores, and the total porosity can be tuned through variation of sample annealing. Dynamic light scattering measurements reveal the presence of COF nanoparticles that grow with time at room temperature, transitioning from a homogeneous suspension to a gel. Finally, we prepare imine COF membranes and measure their rejection of polyethylene glycol (PEG) polymers and oligomers, and these measurements exhibit size-dependent rejection of PEG solutes. This work demonstrates a versatile processing strategy to create crystalline and porous COF materials using solution processing techniques and will greatly advance the development of COFs for various applications.

KEYWORDS: covalent organic frameworks, processing, colloidal nanoparticles, films, membranes, monoliths

INTRODUCTION

Covalent organic frameworks (COFs) are an emerging class of organic nano-porous crystalline materials with tunable pore size, pore architecture, and functionality dictated through the choice of

monomers[1]. Their well-defined, nanoscale pore sizes, high accessible surface areas, and unique optical and electronic properties make them of interest for a variety of applications[2,3,4], including gas storage[5], membrane-based separations[6,7], remediation[8], electronics[9], and catalysis[10].

However, processing COFs for use in various applications remains a significant challenge. COFs are typically prepared via a solvothermal technique that produces an insoluble micro-crystalline powder product, which makes it difficult to process these materials into membranes, films, monoliths, and other bulk shapes[11,12]. While several novel processing strategies have been developed, including solvothermal synthesis on a solid substrate[13], interfacial polymerization[14], powder exfoliation[11], colloidal synthesis[15], solid state processing[16] and gelation[17,18,19], these strategies come with limitations that preclude facile solution processing to make COFs of a desired form and shape. For example, exfoliation of COFs can produce a dispersion of nanosheets[20,21,22] that can be solution-processed into continuous films and coatings[23]. However, such exfoliation strategies produce only a very low concentration of COFs in solution, requiring multiple drop casting and drying steps to produce even thin films[23]. More concentrated stable suspensions of COF nanosheets can be accessed by charge-assisted[24,25,26,27], chemically-assisted[28,29,30] or acid-assisted[11] exfoliation, but these approaches are only applicable to a limited set COF chemistries.

A number of studies have reported routes for processing COFs to produce macroscopic structures such as foams and monoliths[31,32,33,34,35,36,37,38], but many of these methods rely on the inclusion of additives, such as binders[36,37,34,38,31] or templates[35], which remain in the final product. Recent studies have reported successful fabrication of imine COF foams without the use of additives[17,18,19,39]. However, a drawback of these processing approaches is that they involve rapid gelation, which precludes solution processing. For example, Verduzco and coworkers reported a method to make imine COF gels in the polar solvent DMSO and found that gelation occurred within seconds of adding the acid catalyst[19]. While this produced homogeneous gels and foams, rapid gelation prevented solution processing to make films and gels of different forms and shapes.

Solution processing of COFs from a homogeneous solution is an attractive approach for fabrication of homogeneous films, foams, and monoliths. This requires suppressing the heterogenous nucleation and precipitation process characteristic of most COF synthetic methodologies, but strategies for doing this are limited. Dichtel and coworkers optimized the solvent system for the preparation of boronate ester COFs to arrest crystallization and precipitation, resulting in a stable colloidal suspension of crystalline COF nanoparticles[15]. They were able to fabricate free-standing transparent COF films by simply solution casting from this stable suspension[15]. Yaghi and coworkers produced a stable and homogeneous colloidal suspension of imine COFs through the use of protected amine building blocks which could be deprotected *in situ*[13]. They took advantage of this suspension to easily prepare a COF mixed-matrix membrane with COF nanoparticles distributed homogeneously throughout. Jiang and co-workers demonstrated solution processing of amorphous imine polymers, followed by monomer exchange to form a crystalline COF film[40]. While these examples are milestones in COF processing, they are limited to specific COF chemistries and require tedious steps to yield a final crystalline film. More widely applicable facile solution-processing approaches are needed.

Herein, we report an additive-free COF synthesis strategy that suppresses heterogenous precipitation and produces a clear and homogeneous suspension of COF nanoparticles that can subsequently be processed to produce crystalline monoliths, films, and bulk samples. We used the polar solvent dimethylacetamide (DMAc), along with a modified mixing strategy that slows down the growth of COFs and produce a stable suspension of nanoparticles at elevated temperatures ($T \geq 80$ °C). Upon cooling, the nanoparticle suspension forms a crystalline and porous COF gel. This temperature-controlled gelation process enabled us to produce COF films, membranes, and bulk samples using conventional solution-processing techniques. The annealed and dried resulting COF structures were highly crystalline and porous. We demonstrate this strategy for imine and hydrazone COF chemistries of various topologies. We also demonstrate the preparation of COF films of thicknesses ranging from ~100 μm to ~1000 μm and implement our method to produce COF membranes with size-dependent rejection of polyethylene glycol (PEG) polymers. This work demonstrates a simple and versatile

processing strategy to create macroscopic, homogeneous, and crystalline COF scaffolds and will enable more detailed mechanistic studies of COF nucleation and growth mechanisms and significantly advance development of COFs for various applications.

RESULTS AND DISCUSSION

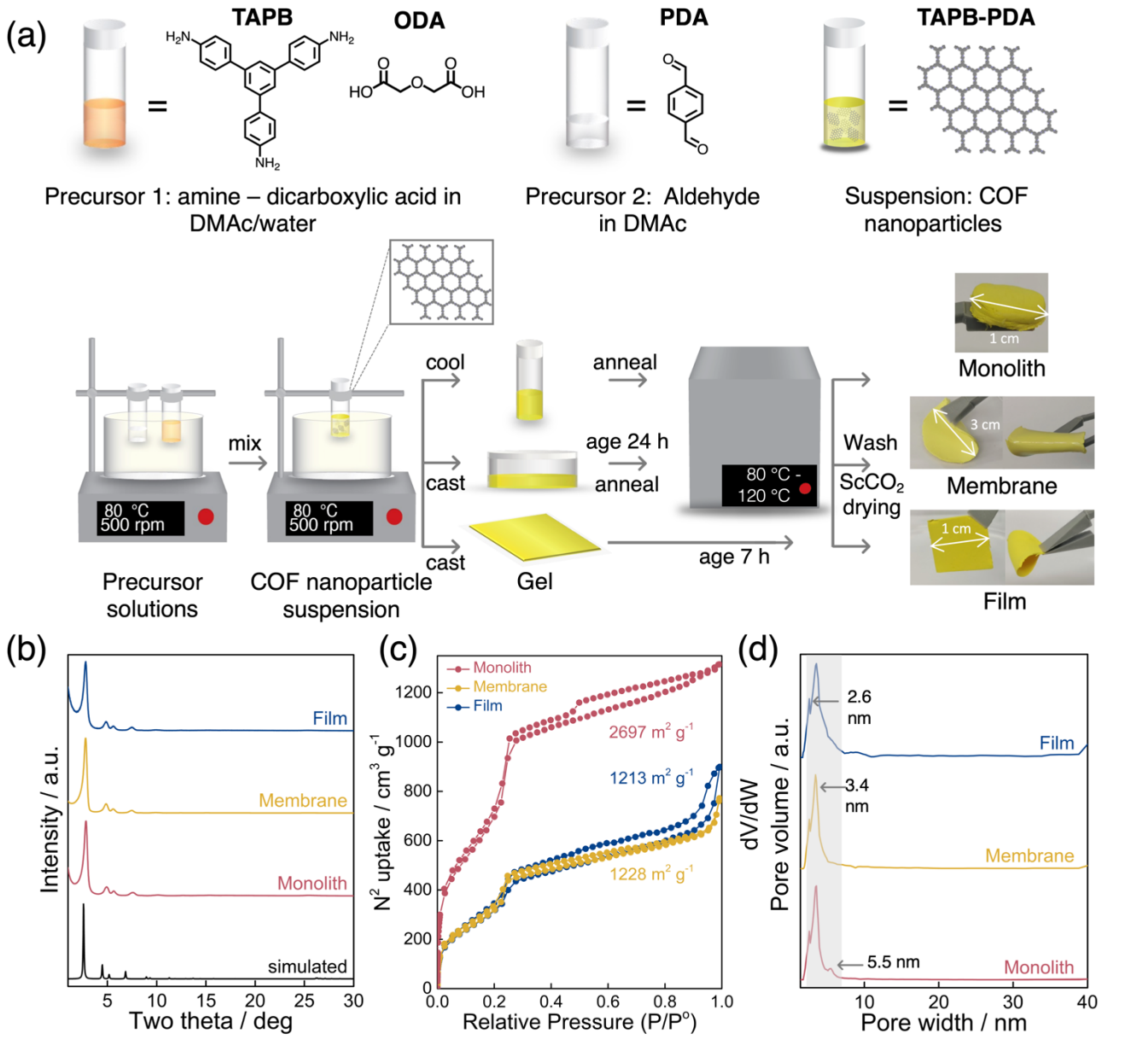

Figure 1. Overview of preparation of stable COF nanoparticle suspension and solution processing to produce crystalline and porous COF monoliths, membranes, and films. a) Schematic for COF synthesis, including the preparation of the precursor solutions in DMAc, mixing at 80°C to produce suspension of COF nanoparticles, and casting and annealing to produce films and bulk samples. b) PXRD patterns of TAPB-PDA monolith, membrane, and film, respectively along with simulated PXRD patterns. c) N_2 adsorption isotherm of TAPB-PDA monolith, membrane and film, respectively , at STP, along with the calculated BET surface areas. d) Pore-size distribution of TAPB-PDA monolith, membrane, and film, respectively, determined through non-local density functional theory (NLDFT).

Modified COF Synthesis Strategy Produces a Stable COF Nanoparticle Suspension. Our goal was to develop a new synthesis and processing approach that would be compatible with solution processing of COFs. The strategy is shown schematically in Fig. 1a for the synthesis of TAPB-PDA COF as a model imine COF using 1,3,5-tris(4-aminophenyl)benzene (TAPB) and terephthalaldehyde (PDA) as building blocks. The rationale behind our modified synthetic strategy was to suppress the precipitation of COF nanoparticles in solution by slowing down their growth and increasing the relative rate of hydrolysis (backward reaction). First, we selected a combination of polar solvents dimethylacetamide (DMAc) and water. DMAc is an excellent solvent for COF monomers and oligomers that reduces the tendency for precipitation and aggregation commonly observed in COF solvothermal synthesis at elevated temperatures. Additionally, the presence of water slows down the rate of growth by increasing the rate of imine hydrolysis in the reversible Schiff base polycondensation reaction[41,42]. To further suppress rapid COF growth and precipitation, we also implemented a modified mixing route where each building block (PDA and TAPB) was dissolved into separate vials prior to heating and mixing (Fig 1a). The acid catalyst was added to the solution of TAPB, resulting in protonation of the amine groups. This further slows down the growth of the imine COFs since the protonated amine groups must first undergo proton transfer before reacting with the di-aldehyde, as has been observed for the salt-mediated synthesis of imine COFs using Bronsted acid[16]. On dropwise addition of PDA (precursor 2) to the TAPB-acid (precursor 1) solution, we observed a clear suspension when kept at 80ºC. We observed the Tyndall effect in the clear suspension indicating the successful formation of stable COF nanoparticles (Fig S1), and this is further supported by dynamic light scattering measurements, discussed in a section that follows. The suspension gelled only when cooled to room temperature and was thermoreversible (SI, Movie 1). Reheating the wet gel (even after aging for 1 day at room temperature) to 120 ºC yielded a clear suspension of nanoparticles with a golden yellow color (Fig S2).

We observed that the solvent system, mixing route, and temperature played a critical role in achieving a clear suspension of imine COF nanoparticles. First, to understand whether water was necessary, we conducted a control experiment under similar conditions but without water. Blending of the precursors

without water resulted in instantaneous gel formation and a COF monolith with poor crystallinity (Fig S3, FWHM = 0.6) rather than a stable nanoparticle suspension. We concluded that water slows down the forward reaction and promotes the backward hydrolysis reaction, slowing down COF growth, nucleation, and precipitation. Our conclusion regarding the effect of water as part of the solvent system is consistent with findings reported by Dichtel and coworkers[42] and Lotsch and coworkers[41]. We also tested the effect of solvent by repeating our process using DMSO instead of DMAc. With DMSO, a non-homogenous gel immediately formed rather than a stable suspension of COF nanoparticles. We attribute this to the higher polarity of DMSO solvent that increases the rate of the Schiff condensation reaction relative to the hydrolysis reaction. Furthermore, we found that it was important to add acid to the solution containing the tri-amino monomer TAPB. If acid was added to the aldehyde precursor PDA rather than the tri-amino monomer TAPB, a gel formed quickly on blending the solutions. We attribute this to the protonation of the primary amines (see interaction maps of TAPB and ODA in the Supporting Information Fig S4), which inhibits the Schiff base reaction upon blending the precursor solutions.

To characterize the crystallinity of the COF particles suspended in solution, we precipitated the nanoparticles from the suspension using hexane and performed powder X-ray diffraction (PXRD) measurements (see procedure described in the Supplemental Information in Fig S5). The nanoparticles showed diffraction peaks at 2.9º and 4.9º attributed to the (100) and (110) planes, respectively, with a full-width-at-half-maximum (FWHM) of 0.56 (Fig S5), confirming the presence of COF nanocrystals in the suspension. Scanning electron microscopy (SEM) analysis of these nanoparticles revealed the formation of approximately 50 nm COF nanowires that cluster to form nanospheres upon precipitation (Fig. S6). These measurements demonstrate that our modified synthesis approach produces a suspension of crystalline COF nanoparticles.

Processing of COF Nanoparticle Suspension. This modified synthetic methodology enabled the preparation of COF monoliths, membranes, and films using facile solution processing strategies (Fig. 1a). We prepared COF monoliths by first cooling the COF nanoparticle suspension to room temperature, resulting in the formation of a COF gel. The gel was dried and thermally annealed at 90ºC for 3 days to

produce a dry COF monolith. The COF monoliths were then solvent exchanged with THF followed by ethanol to wash away unreacted precursors and then dried using supercritical CO_2 ($ScCO_2$) to yield crystalline and porous monoliths. To produce COF membranes, the stable nanoparticle suspension was poured into a borosilicate container at room temperature, after which gelation occurred (see Supporting Information Movie S2). To ensure complete reaction and removal of residual solvent, the wet gel was aged at ambient conditions for one day, heated to 80ºC for 3h, and then heated to 120ºC for 2 hours. COF membranes were then solvent exchanged with THF followed by ethanol to wash away unreacted precursors and then dried using $ScCO_2$ to yield crystalline and porous membranes. The resulting COF membrane possessed excellent mechanical integrity and was easy to handle and remove from the substrate. Thinner film samples (~100 μm) were produced by drop casting a desired volume of nanoparticle suspension onto a glass substrate producing a COF gel (Fig 1a). The gel was subsequently aged for 7 h at ambient conditions and was removed from the glass substrate by immersion in water to produce a free-floating COF film. The thin film was solvent exchanged with THF and ethanol and then dried using $ScCO_2$ yielding a fully dry thin film. The thickness of the film was tuned by simply varying the volume of solution deposited on the substrate, down to ~120 μm (Table S1). Detailed procedures for producing monoliths, membranes, and films are provided in the Supplementary Information notes 1.3-1.5.

Our first attempts at COF monolith synthesis relied on 6 M acetic acid as the catalyst, but the resulting COF product had poor crystallinity (see procedure described in the Supplemental Information and PXRD patterns in Fig S7). To improve the crystallinity of the final product, we explored the use of alternative acid catalysts that could self-assemble in solution and increase the final crystallinity. This was motivated by prior work with thermo-reversible supramolecular two component organo-gels which can be formed by the self-assembly of dicarboxylic acids and primary alkyl amines in polar solvents[43]. We hypothesized that a similar self-assembly process between COF amine monomer and acid catalyst could enhance the final crystallinity of imine COFs. To test our hypothesis, we blended TAPB with dicarboxylic acid (ODA) or acetic acid (AcOH) respectively, in DMAc at both 80°C and room

temperature (22°C) (Table S2). AcOH and ODA were each added in stoichiometric ratio with respect to amine functionality (1:3 TAPB:AcOH and 2:3 TAPB:ODA). The TAPB-ODA solution showed a thermo-reversible solution-to-gel transition, reflecting the formation of supramolecular organic gels at room temperature (Table S2). This thermo-reversibility is attributed to the self-assembly process between COF amine monomeric units and dicarboxylic acid. On the contrary, TAPB-AcOH solution in DMAc failed to gel at room temperature. Furthermore, we found that the ODA acid catalyst improved the crystallinity of the final COF materials. The PXRD patterns of the resulting TAPB-PDA monoliths, membranes, and films prepared using ODA showed excellent crystallinity and matched the simulated pattern of TAPB-PDA imine COF (Fig 1b). The solid COF samples showed diffraction peaks at 2.9º, 4.9º and 5.6º attributed to the (100), (110), and (200) planes, respectively. The (100) peak of TAPB-PDA monoliths and membranes had a FWHM of 0.38, confirming the excellent crystallinity of these samples. Thin film samples had a broader FWHM ($FWHM_{100}$=0.429) for the most intense (100) peak due to annealing at room temperature conditions. Fourier transform infrared (FTIR) spectroscopy analysis of TAPB-PDA COF monoliths, membranes, and films confirmed the successful formation of the imine bond (C=N) with a stretching band at ~1617 cm^{-1} (Fig S8). Only very weak amino (~3359 cm^{-1}) and carbonyl (~1685 cm^{-1}) group vibrations were present in the IR spectra, due to the presence of terminal unreacted end groups within COF layers.

To gain insight into the porosity of the fabricated structures, N_2 adsorption studies were performed on TAPB-PDA COF monoliths, membranes, and films at 77K and 1 atm (Fig 1c). The calculated Brunauer-Emmett-Teller (BET) surface areas for TAPB-PDA monoliths, membranes, and films were 2697 $m^2 g^{-1}$, 1228 $m^2 g^{-1}$ and 1213 $m^2 g^{-1}$, respectively (Fig 1c). The extremely high BET surface area of the monolith (2697 $m^2 g^{-1}$) indicates that this sample approaches the Connolly theoretical surface area of TAPB-PDA COF[44]. We attributed the difference in surface areas between the monolithic and film scaffolds to the improved imine exchange due to extended heating periods for the monoliths. All isotherms showed a steep increase at low relative pressure (below 0.3) followed by monotonic gas uptake confirming the presence of both micropores and mesopores within the COF samples. There was

a clear hysteresis between the adsorption and desorption loops of all fabricated TAPB-PDA COF structures at high relative pressure, which we attribute to pore network effects[45]. The N_2 adsorption isotherm of TAPB-PDA thin film showed hysteresis between adsorption and desorption loops even at lower relative pressures.

We estimated the pore sizes of COF monolith, membrane, and film samples using the non-local density functional theory (NLDFT) model. This model showed that all have a predominant pore size of 3.4 nm, which corresponds to the expected crystalline COF structure (Fig 1d). All samples also possessed pores at 2.6 nm, which we attribute to interparticle aggregation[18,45]. Monolith COF samples, showed additional pores with s 5.5 nm width, which could possibly be a result of gate opening phenomena due to guest induced structural transitions (pore expansion)[18,45]. These results are consistent with previous reports on TAPB-PDA COF foams[18,19]. To further understand the differences between these samples, we performed total porosity analysis, which takes into account both microstructural and structural porosities (see Supplementary Note 1.2.10 for details on total porosity estimation method). These estimates showed that monoliths and membranes have a total porosity ~97%, while film samples have a lower total porosity of ~86% (Table S3). Comparing these values with previous reports on COF foams[18], the microstructural porosity of all our COF samples (49-90%) is much lower than that previously reported for TAPB-PDA foams (95.5%). We attribute this to reduced percentage of macro-voids in the COF samples fabricated using our modified synthetic strategy. Moreover, our modified synthetic route enables the control of macro-void percentage (49-90%) by varying annealing strategy of the sample (see Table S3). This enables tuning and optimization of total porosity for a desired application.

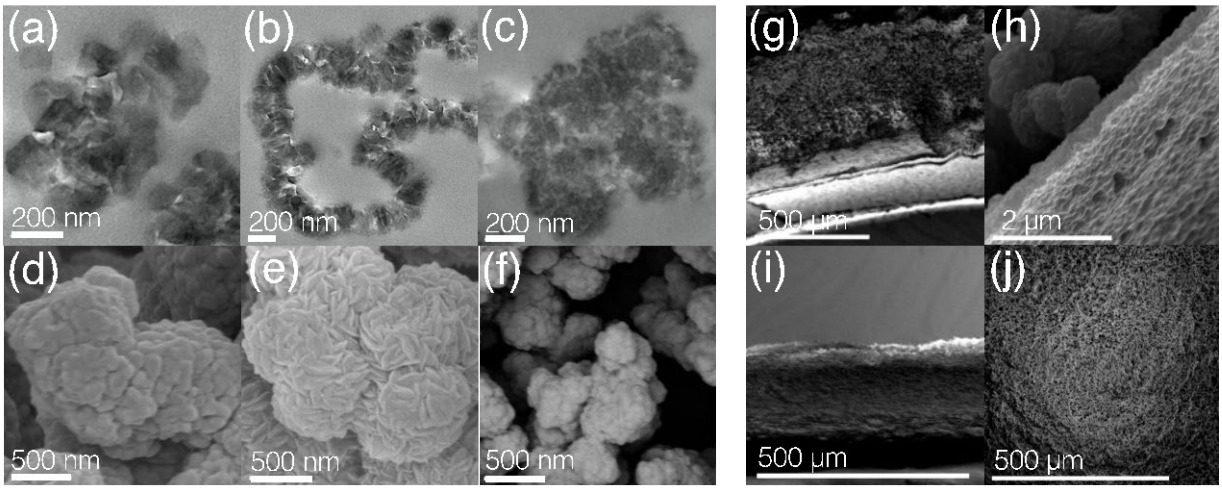

Figure 2. Microstructure of COF monoliths, membranes, and films. a, b, c, TEM and d, e, f, SEM images of TAPB-PDA monolith, membrane and film, respectively. g,h, Cross-sectional SEM images of TAPB-PDA membrane. i, Cross-sectional and j, Top view SEM images of TAPB-PDA film.

To understand the difference in surface areas and crystallinities observed for the various TAPB-PDA COF structures produced using our modified approach, we performed transmission electron microscopy (TEM) and scanning electron microscopy (SEM) analysis of monoliths, membranes, and films. TEM images of TAPB-PDA COF samples revealed the formation of interconnected nanoparticles (Fig 2a-c), in contrast to aggregated particles observed for powder TAPB-PDA obtained from the conventional solvothermal route (Fig S9). SEM images of the TAPB-PDA monolith showed the formation of clusters comprised of non-uniform particles with an average particle size of ~190 nm (Fig 2d). In contrast, SEM images of the TAPB-PDA membrane indicate the formation of uniform leaf-like particles with an average particle size of ~200 nm assembled into interconnected spherical clusters (Fig 2e). TEM analysis suggests these spherical clusters are hollow from the inside (Fig 2b and Fig S10). SEM images of TAPB-PDA film also revealed the formation of clusters that were comprised of particles with an average particle size of ~80 nm (Fig 2f). We attribute the smaller average particle size of film samples in comparison to monolithic and membrane samples (~ 200 nm) to the room temperature annealing stage. Our results are consistent with previous findings by Lotsch[46] and co-workers that showed that imine COFs synthesized at room temperature consist of smaller particle sizes (~50 nm) in comparison to those synthesized at a higher temperature of 120 °C (~100 nm). TEM analysis of these particles revealed

the formation of a partially hollow structure (Fig 2c). The control over microstructure of monoliths and films is important for many applications, including both gas and liquid separation and storage, and our approach can be used to tune the microstructure and particle size distribution by simply varying the annealing conditions.

To validate the quality of the fabricated membranes and films for use in applications, we performed surface and cross-sectional SEM analysis (Fig 2g-j). Cross-sectional SEM images of TAPB-PDA membranes revealed the formation of a thin dense film on the bottom side, and a foam like structure on the top side (Fig 2g,h). This heterogeneous structure is attributed to a concentration gradient across the membrane that arises during thermal annealing where ligand volatilization from the top surface is greater than the bottom surface[47]. Cross-sectional SEM images of film samples aged at room temperature without any thermal treatment shows the formation of foam-like structure across the film (Fig 2i). The surface SEM image further confirms the foam like structure on the top of the film sample (Fig 2j). This difference in microstructure of film and membrane samples induced by thermal annealing results in variation of the density of the final structure (Table S3). The fabricated films and membranes are very light and have a calculated density of approximately 0.2 and 0.038 g cm^{-3}, respectively. The membranes have a much lower density compared to the thin films due to their hollow particle structure and asynchronous crystallization induced by thermal treatment of the membranes yielding more microstructural porosity (Table S3). Interestingly, this difference in morphology has a very large impact on the surface wettability. Contact angle measuremens (Fig. S11) show that the top porous layer is hydrophobic (water contact angle 121°) while the more dense bottom layer is hydrophilic (water contact angle 46°). We attribute this large difference in wettability to the dependence on the wetting state of the droplet, which depends strongly on surface roughness[48].

Mechanical properties of the membranes and films were assessed using tensile testing (Fig S12). Stress-strain relationships showed that the membrane samples have a higher tensile modulus (0.009 MPa) and tensile strength (0.038 MPa) compared to the thin film samples (0.001 MPa and 0.009 MPa,

respectively). We attribute this difference in mechanical properties between membrane and film samples to variations in their morphologies that arises due to different heating conditions and particle sizes (Fig 2a-f), and these measurements reflect advantages in terms of mechanical properties that result from the unique morphology of the COF membranes.

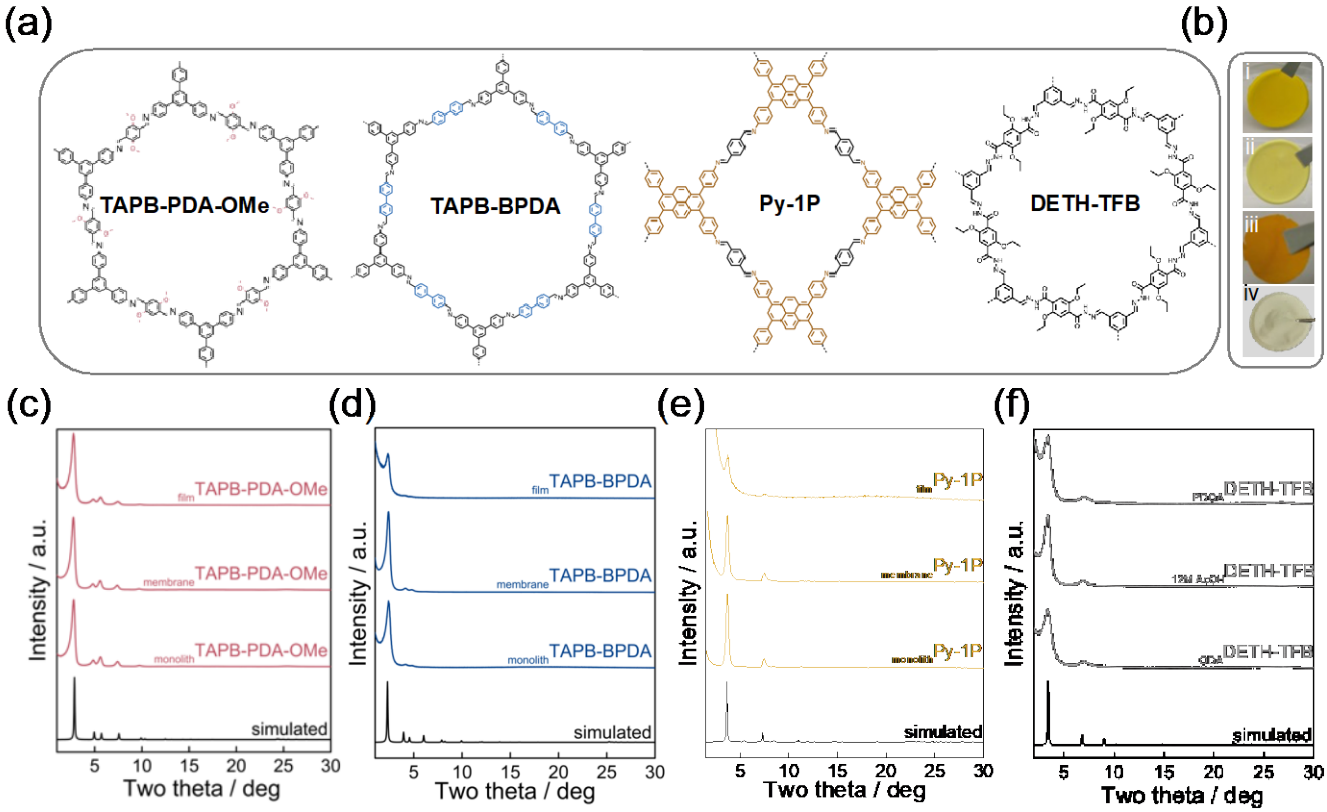

Figure 3. Solution-based synthesis of imine and hydrazone COFs. a, Chemical structure of imine and hydrazone frameworks synthesized using modified synthesis strategy. b, Digital photograph of i) TAPB-PDA-OMe (orange), ii) TAPB-BPDA (pale yellow), iii) Py-1P (brown), and iv) DETH-TFB (white) membranes. c, PXRD patterns of TAPB-PDA-OMe monolith, membrane, and film, respectively along with simulated PXRD pattern. d, PXRD patterns of TAPB-BPDA monolith, membrane, and film respectively along with simulated PXRD pattern. e, PXRD patterns of Py-1P monolith, membrane, and film respectively along with simulated PXRD pattern. f, PXRD patterns of DETH-TFB monolith, fabricated using various catalysts including ODA, PDOA, and AcOH, along with simulated PXRD pattern.

Next, we demonstrated the versatility of our modified synthetic route through the preparation three other imine COF chemistries: TAPB-BPDA, TAPB-PDA-OMe and Py-1P (Fig 3a). TAPB-BPDA and TAPB-PDA-OMe have a hexagonal topology, while Py-1P has a rhombic topology. TAPB-BPDA has a very large pore size (4.01 nm) and is a fragile framework highly susceptible to pore collapse. On the other hand, TAPB-PDA-OMe is a robust framework due to resonance effect induced by methoxy side

groups that promote framework crystallization and pi-pi stacking[49]. First, we verified the self-assembly between all amine COF monomers and ODA catalyst in DMAc solvent by performing vial inversion tests at elevated temperature (80°C) and room temperature (22°C) (Table S2). All tested amine monomers formed a thermoreversible gel in solution with ODA and in DMAc (Table S2). Next, we produced monoliths, membranes, and films of various thicknesses of TAPB-BPDA, TAPB-PDA-OMe, and Py-1P (see supplementary notes 1.3-1.5 for synthetic details, Fig S13, and Table S4). FTIR analysis confirmed the successful formation of TAPB-PDA-OMe, TAPB-BPDA and Py-1P scaffolds, respectively (Fig S14-16). PXRD patterns of the monolith and casted films of TAPB-PDA-OMe, TAPB-BPDA, and Py-1P compared well to simulated patterns (Fig 3c-e) and confirmed the excellent crystallinities of synthesized COF structures. The scaffolds of the frameworks possessed excellent surface areas as confirmed by N_2 adsorption isotherms (Fig S17-20). For example, TAPB-BPDA, and TAPB-PDA-OMe membranes had BET surface areas of 1198 $m^2\ g^{-1}$ and 2919 $m^2\ g^{-1}$, respectively, both all of which are greater than their reported powder counterparts[50,44](Fig S17).

The fabricated membranes were homogenous, with no apparent macroscopic defects (digital photographs in Fig 3b) and contained a hierarchical microstructure (see SEM analysis in the Supporting Information Fig S21-22). The mechanical properties of films and membranes were assessed using tensile testing (Table S5), and we found that the TAPB-BPDA membrane had a greater modulus and tensile strength compared to TAPB-PDA-OMe membrane. On the other hand, Py-1P had a greater tensile strength but a lower modulus compared to TAPB-BPDA COF membrane. These results demonstrate that our modified synthesis approach is effective for the preparation of a variety of imine-linked COF membranes and films.

We also tested our modified synthetic route for the fabrication of hydrazone-linked COFs, which exhibit excellent thermal and chemical stabilities[51]. We applied our modified COF synthesis to the preparation of COF-42 using DETH and TFB monomers (Figure 3a). Following our reported procedure, we tested the effect of various catalysts for the preparation of COF-42 monoliths, including 12 M

AcOH, ODA, and 1,5-pentanedioic acid (PDOA) (See supplementary note 1.3.5 for details on synthesis). Surprisingly, all fabricated samples showed excellent crystallinities and matched with simulated patterns (Fig 3f). However, the suspension gelled instantly upon mixing amine and aldehyde precursors at elevated temperature for ODA and AcOH catalyzed samples, hampering solution processing of suspensions to films and membranes. We attribute this to the hydrogen bonding between the COF layers that promotes the instant gelation of nanoparticles in DMAc solvent. On the other hand, samples prepared using PDOA as a catalyst gelled only upon cooling, enabling solution processing of COF nanoparticle suspension to a crystalline COF membrane (Fig 3b-iv, Fig S23).

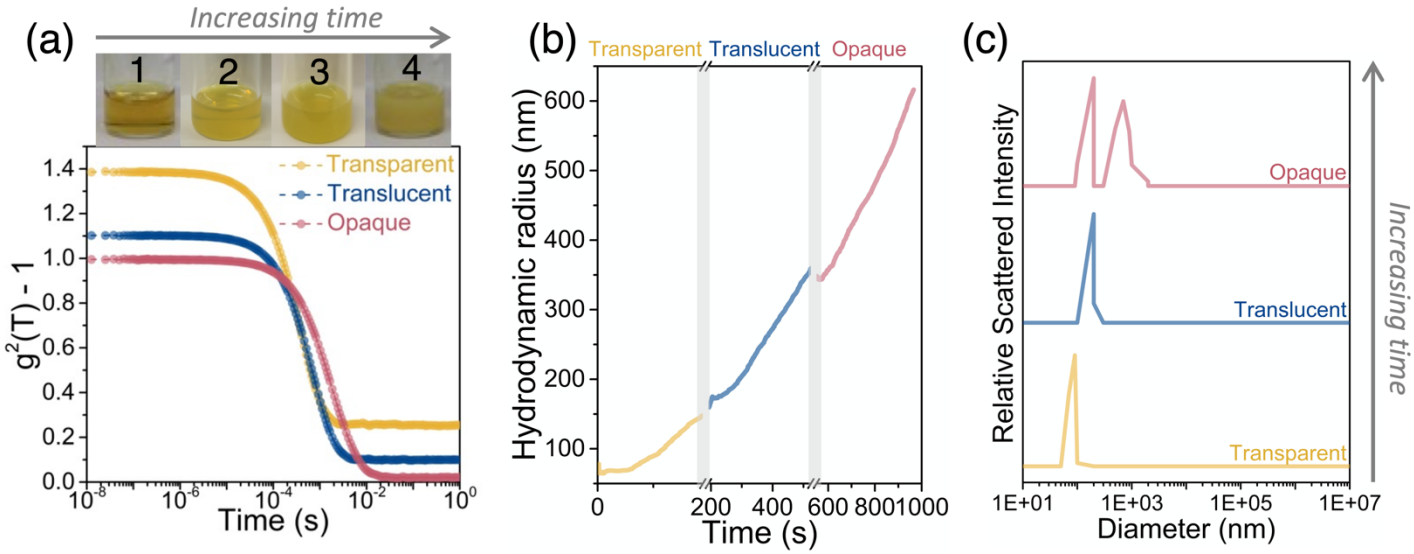

Figure 4. Dynamic light scattering (DLS) analysis of COF nanoparticle suspension. a, Correlation function vs time derived from dynamic light scattering performed on clear suspension of TAPB-PDA imine COF nanoparticles until it gels (transparent-translucent-opaque). Images showing colloidal suspension transparency evolution as particle size increases. b, Particle size evolution as colloidal nanoparticle suspension transitions from transparent to translucent and eventually opaque before it gels . c, Variation of statistical particle size distribution as colloidal suspension transitions from transparent to translucent and eventually opaque before it gels.

Particle Growth Analysis. We used dynamic light scattering (DLS) to analyze the evolution of particle size and size distribution as the suspension cooled to ambient temperature and gradually formed a gel. This enabled us to track particle evolution for the initially clear suspension as the solution became translucent and eventually opaque (Fig. 4). DLS measurements confirmed the presence of non-isotropic nanoparticles in the optically clear dispersion (Fig. S24). The particles were approximately 100 nm, but

these particles steadily grew in size as the dispersion cooled (Fig. 4b). The scattered intensity increased continuously with time, and the dispersion transitioned from optically clear, to translucent, and then opaque. Analysis of the scattered intensity from the clear and translucent suspensions revealed a single exponential decay (Fig. 4a) and a monodisperse particle distribution (Fig. 4c) that increased in size with time. The particle size ranged from approximately 100 nm for the clear suspension, 300 nm for the translucent suspension, and greater than 700 nm for the opaque sample (Fig. 4c). These measurements clearly demonstrate that our synthesis method produces an optically clear and stable suspension of COF nanoparticles, which grow upon cooling and subsequently gel.

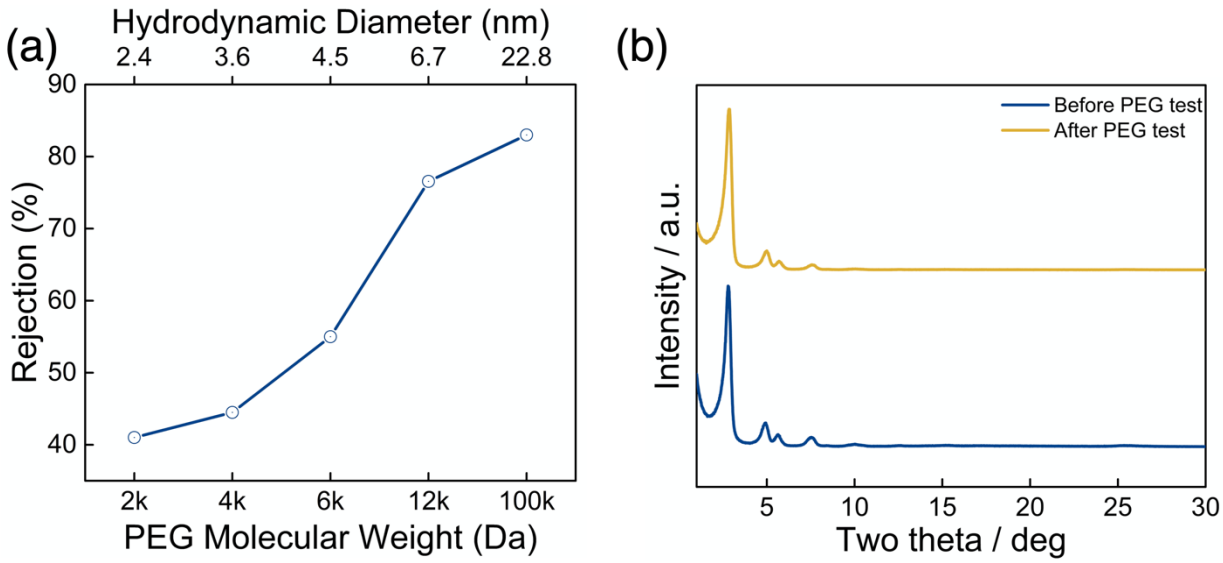

Figure 5. Rejection performance of TAPB-PDA membrane. a, PEG rejection by TAPB-PDA membrane. b, PXRD pattern of TAPB-PDA membrane before and after the PEG rejection tests, respectively.

COF gel membrane rejection performance. We produced uniform COF membranes of a desired size by solution casting onto a petri dish and tested their performance in size exclusion experiments. We produced membranes with thickness of approximately ~ 700 μm and quantified the rejection of poly(ethylene glycol) (PEG) oligomers and polymers varying in molecular weight from 2000 to 100,000 g/mol, corresponding to hydrodynamic sizes ranging from 2.4 nm to 22.8 nm (see Table S6). The

membranes were placed in a dead-end cell (Amicon 1080, Fig S25) and pressurized using N_2 gas at 150 kPa. A separate stock solution in DI water was prepared for each PEG solute at a concentration of 0.1 g L^{-1}. Each solution was then passed through the COF membrane using the procedure described in the Experimental Section. Solutions were analyzed using a total organic carbon analyzer (TOC) to determine the concentrations of PEG that passed through the COF membrane.

The TAPB-PDA membrane showed a clear dependence of rejection on the size of the solute (Fig 4a), with the highest rejection measured for the largest PEG solute. However, less than 100 % rejection was observed across all solutes measured, despite the sizes of the solute being as large as 22.8 nm, much larger than the COF pore size (3.4 nm). This suggests that the COF membranes contain defects and/or macropores that allow for the permeation of large solutes through the membrane. The estimated macro-void fraction of the membranes was ~92% of the total porosity, and this could be tuned by varying annealing strategy used or compacting the membrane prior to testing. Nevertheless, the COF membranes exhibited a number of attractive features. The membranes maintained their structural integrity and microstructural properties after the rejection experiments, with no loss of crystallinity observed after the permeation tests (see Fig 4b). No visible cracks or defects were apparent on the membranes after 14 cycles use, indicating their robustness and suitability for use in pressure-driven separations. Finally, we observed a trend in rejection with PEG solute size, suggesting that further tailoring the microstructure to limit macropores or defects could improve performance. The membranes also had a very high flux of 355.8 L m^{-2} h^{-1} at 1 atm, which we attribute to the porosity and surface area of the membrane.

CONCLUSIONS

We demonstrated a facile solution–processing strategy of imine COFs enabled through a modified synthetic approach that produces a homogeneous and stable suspension of COF nanoparticles. The suspension is stable at elevated temperatures, and upon cooling produces a gel. The temperature-controlled gelation from a homogeneous nanoparticle suspension enabled us to easily produce films,

membranes, and bulk samples using conventional solution-processing techniques. In addition to facilitating the processing of COFs for various applications, this modified synthetic route also produces highly crystalline, porous, and hierarchically structured COFs, and the approach is compatible with imine and hydrazone COFs of various topologies. This work demonstrates a simple and versatile processing route to produce macroscopic, homogeneous, and crystalline COF scaffolds and will significantly advance the development of COFs for various applications including energy storage and separation. We anticipate the access to a clear suspension of COF colloids will enable the more careful study of COF nucleation and growth mechanisms and facilitate access to COF films, foams, and membranes with a variety of chemistries.

ASSOCIATED CONTENT

Supporting Information

Supporting Information is available free of charge online. Supporting Information includes details on materials and methods, photographs of sample solutions, gels, and membranes, XRD, FTIR, SEM, nitrogen sorption, dynamic light scattering, and mechanical analysis data, and videos of the COF gelation process (AVI).

AUTHOR INFORMATION

Corresponding Author

*(R.V.) E-mail: rafaelv@rice.edu.

ORCID

Safiya Khalil: 0000-0001-6083-7927

Rafael Verduzco: 0000-0002-3649-3455

Notes

The authors declare no competing financial interest.

ACKNOWLEDGMENT

SK acknowledges support from the Ministry of Education of United Arab Emirates (UAE). This work was supported in part by the NSF Nanosystems Engineering Research Center for Nanotechnology-Enabled Water Treatment (EEC-1449500).

REFERENCES

(1) Côté, A. P.; Benin, A. I.; Ockwig, N. W.; O'Keeffe, M.; Matzger, A. J.; Yaghi, O. M. Porous, Crystalline, Covalent Organic Frameworks. *Science* **2005**, *310* (5751), 1166–1170. https://doi.org/10.1126/science.1120411.

(2) Lohse, M. S.; Bein, T. Covalent Organic Frameworks: Structures, Synthesis, and Applications. *Adv. Funct. Mater.* **2018**, *28* (33), 1705553. https://doi.org/10.1002/adfm.201705553.

(3) Huang, N.; Wang, P.; Jiang, D. Covalent Organic Frameworks: A Materials Platform for Structural and Functional Designs. *Nat. Rev. Mater.* **2016**, *1* (10), 16068. https://doi.org/10.1038/natrevmats.2016.68.

(4) Geng, K.; He, T.; Liu, R.; Tan, K. T.; Li, Z.; Tao, S.; Gong, Y.; Jiang, Q.; Jiang, D. Covalent Organic Frameworks: Design, Synthesis, and Functions. *Chem. Rev.* **2020**, ASAP. https://doi.org/10.1021/acs.chemrev.9b00550.

(5) Ozdemir, J.; Mosleh, I.; Abolhassani, M.; Greenlee, L. F.; Beitle, R. R.; Beyzavi, M. H. Covalent Organic Frameworks for the Capture, Fixation, or Reduction of CO2. *Front. Energy Res.* **2019**, *7*, 77. https://doi.org/10.3389/fenrg.2019.00077.

(6) Yuan, S.; Li, X.; Zhu, J.; Zhang, G.; Van Puyvelde, P.; Van Der Bruggen, B. Covalent Organic

Frameworks for Membrane Separation. *Chem. Soc. Rev.* **2019**, *48* (10), 2665–2681. https://doi.org/10.1039/c8cs00919h.

(7) Wang, Z.; Zhang, S.; Chen, Y.; Zhang, Z.; Ma, S. Covalent Organic Frameworks for Separation Applications. *Chem. Soc. Rev. 49*, 708–735. https://doi.org/10.1039/c9cs00827f.

(8) Mohammed, A. K.; Shetty, D. Macroscopic Covalent Organic Framework Architectures for Water Remediation. *Environ. Sci. Water Res. Technol.* **2021**, *7* (11), 1895–1927. https://doi.org/10.1039/D1EW00408E.

(9) Bian, G.; Yin, J.; Zhu, J. Recent Advances on Conductive 2D Covalent Organic Frameworks. *Small* **2021**, *17* (22). https://doi.org/10.1002/SMLL.202006043.

(10) Guo, J.; Jiang, D. Covalent Organic Frameworks for Heterogeneous Catalysis: Principle, Current Status, and Challenges. *ACS Cent. Sci.* **2020**, *6* (6), 869–879. https://doi.org/10.1021/ACSCENTSCI.0C00463.

(11) Burke, D. W.; Sun, C.; Castano, I.; Flanders, N. C.; Evans, A. M.; Vitaku, E.; McLeod, D. C.; Lambeth, R. H.; Chen, L. X.; Gianneschi, N. C.; Dichtel, W. R. Acid Exfoliation of Imine-Linked Covalent Organic Frameworks Enables Solution Processing into Crystalline Thin Films. *Angew. Chem. Int. Ed.* **2020**, *59* (13), 5165–5171. https://doi.org/10.1002/anie.201913975.

(12) David Rodríguez-San-Miguel, S.; Zamora, F.; Rodrí guez-San-Miguel, D.; lix Zamora, F. Processing of Covalent Organic Frameworks: An Ingredient for a Material to Succeed. *Chem. Soc. Rev.* **2019**, *48*, 4375–4386. https://doi.org/10.1039/c9cs00258h.

(13) Zhao, Y.; Guo, L.; Felipe, G.; Ma, Y.; Liu, Z.; Zhu, C.; Lyu, H.; Trickett, C. A.; Kapustin, E. A.; Terasaki, O.; Yaghi, O. M. A Synthetic Route for Crystals of Woven Structures, Uniform Nanocrystals, and Thin Films of Imine Covalent Organic Frameworks. *J. Am. Chem. Soc.* **2017**, *139*, 13166–13172. https://doi.org/10.1021/jacs.7b07457.

(14) Matsumoto, M.; Valentino, L.; Stiehl, G. M.; Balch, H. B.; Corcos, A. R.; Wang, F.; Ralph, D. C.; Mariñas, B. J.; Dichtel, W. R. Lewis-Acid-Catalyzed Interfacial Polymerization of Covalent Organic Framework Films. *Chem* **2018**, *4*, 308–317. https://doi.org/10.1016/j.chempr.2017.12.011.

(15) Smith, B. J.; Parent, L. R.; Overholts, A. C.; Beaucage, P. A.; Bisbey, R. P.; Chavez, A. D.; Hwang, N.; Park, C.; Evans, A. M.; Gianneschi, N. C.; Dichtel, W. R. Colloidal Covalent Organic Frameworks. *ACS Cent. Sci.* **2017**, *3* (1), 58–65. https://doi.org/10.1021/acscentsci.6b00331.

(16) Karak, S.; Kandambeth, S.; Biswal, B. P.; Sasmal, H. S.; Kumar, S.; Pachfule, P.; Banerjee, R. Constructing Ultraporous Covalent Organic Frameworks in Seconds via an Organic Terracotta Process. *J. Am. Chem. Soc.* **2017**, *139* (5), 1856–1862. https://doi.org/10.1021/jacs.6b08815.

(17) Carrington, M. E.; Rampal, N.; Madden, D. G.; O'Nolan, D.; Casati, N. P. M.; Divitini, G.; Cepitis, R.; Martín-Illán, J. Á.; Çamur, C.; Silvestre-Albero, J.; Zamora, F.; Taraskin, S.; Chapman, K.; Fairen-Jimenez, D. Sol-Gel Processing of a Covalent-Organic Framework for the Generation of Hierarchically Porous Monolithic Adsorbents. *ChemRxiv.* **2021**. https://doi.org/10.26434/chemrxiv.14381378.v1.

(18) Martín-illán, J. Á.; Rodríguez-san-miguel, D.; Castillo, O.; Beobide, G.; Perez-Carvajal, J.; Imaz, I.; Maspoch, D.; Zamora, F. Macroscopic Ultralight Aerogel Monoliths of Imine-Based Covalent Organic Frameworks. *Angew. Chem. Int. Ed.* **2021**, *60*, 1–12. https://doi.org/10.1002/anie.202100881.

(19) Zhu, D.; Zhu, Y.; Yan, Q.; Barnes, M.; Liu, F.; Yu, P.; Tseng, C.-P.; Tjahjono, N.; Huang, P.-C.; Rahman, M. M.; Egap, E.; Ajayan, P. M.; Verduzco, R. Pure Crystalline Covalent Organic Framework Aerogels. *Chem. Mater.* **2021**, *33* (11), 4216–4224. https://doi.org/10.1021/acs.chemmater.1c01122.

(20) Wang, S.; Wang, Q.; Shao, P.; Han, Y.; Gao, X.; Ma, L.; Yuan, S.; Ma, X.; Zhou, J.; Feng, X.; Wang, B. Exfoliation of Covalent Organic Frameworks into Few-Layer Redox-Active Nanosheets as Cathode Materials for Lithium-Ion Batteries. *J. Am. Chem. Soc.* **2017**, *139* (12), 4258–4261. https://doi.org/10.1021/jacs.7b02648.

(21) Peng, Y.; Huang, Y.; Zhu, Y.; Chen, B.; Wang, L.; Lai, Z.; Zhang, Z.; Zhao, M.; Tan, C.; Yang, N.; Shao, F.; Han, Y.; Zhang, H. Ultrathin Two-Dimensional Covalent Organic Framework Nanosheets: Preparation and Application in Highly Sensitive and Selective DNA Detection. *J. Am. Chem. Soc.* **2017**, *139* (25), 8698–8704. https://doi.org/10.1021/jacs.7b04096.

(22) Berlanga, I.; Rube´n, M.-B.; Zamora, F. Tuning Delamination of Layered Covalent Organic Frameworks through Structural Design. *Chem. Commun.* **2012**, *48*, 7976–7978. https://doi.org/10.1039/c2cc32187d.

(23) Li, G.; Zhang, K.; Tsuru, T. Two-Dimensional Covalent Organic Framework (COF) Membranes Fabricated via the Assembly of Exfoliated COF Nanosheets. *ACS Appl. Mater. Interfaces.* **2017**, *9* (10), 8433–8436. https://doi.org/10.1021/acsami.6b15752.

(24) Li, X.; Hou, Q.; Huang, W.; Xu, H.-S.; Wang, X.; Yu, W.; Li, R.; Zhang, K.; Wang, L.; Chen, Z.; Xie, K.; Loh, K. P. Solution-Processable Covalent Organic Framework Electrolytes for All-Solid-State Li− Organic Batteries. *ACS Energy Lett.* **2020**, *5* (11), 3498–3506. https://doi.org/10.1021/acsenergylett.0c01889.

(25) Peng, P.; Shi, L.; Huo, F.; Zhang, S.; Mi, C.; Cheng, Y.; Xiang, Z. In Situ Charge Exfoliated Soluble Covalent Organic Framework Directly Used for Zn-Air Flow Battery. *ACS Nano* **2019**, *13* (1), 878–884. https://doi.org/10.1021/acsnano.8b08667.

(26) Mitra, S.; Kandambeth, S.; Biswal, B. P.; Mohammed, A. K.; Choudhury, C. K.; Mehta, M.; Kaur, G.; Banerjee, S.; Prabhune, A.; Verma, S.; Roy, S.; Kharul, U. K.; Banerjee, R. Self-Exfoliated Guanidinium-Based Ionic Covalent Organic Nanosheets (ICONs). *J. Am. Chem. Soc.*

2016, *138* (8), 2823–2828. https://doi.org/10.1021/jacs.5b13533.

(27) Wang, L.; Zeng, C.; Xu, H.; Yin, P.; Chen, D.; Deng, J.; Li, M.; Zheng, N.; Gu, C.; Ma, Y. A Highly Soluble, Crystalline Covalent Organic Framework Compatible with Device Implementation. *Chem. Sci.* **2019**, *10*, 1023–1028. https://doi.org/10.1039/c8sc04255a.

(28) Khayum, M. A.; Kandambeth, S.; Mitra, S.; Nair, S. B.; Das, A.; Nagane, S. S.; Mukherjee, R.; Banerjee, R. Chemically Delaminated Free-Standing Ultrathin Covalent Organic Nanosheets. *Angew. Chem. Int. Ed.* **2016**, *55* (50), 15604–15608. https://doi.org/10.1002/anie.201607812.

(29) Mitra, S.; Sasmal, H. S.; Kundu, T.; Kandambeth, S.; Illath, K.; Díaz, D. D.; Banerjee, R. Targeted Drug Delivery in Covalent Organic Nanosheets (CONs) via Sequential Postsynthetic Modification. *J. Am. Chem. Soc.* **2017**, *139* (12), 4513–4520. https://doi.org/10.1021/jacs.7b00925.

(30) Chen, X.; Li, Y.; Wang, L.; Xu, Y.; Nie, A.; Li, Q.; Wu, F.; Sun, W.; Zhang, X.; Vajtai, R.; Ajayan, P. M.; Chen, L.; Wang, Y. High-Lithium-Affinity Chemically Exfoliated 2D Covalent Organic Frameworks. *Adv. Mater.* **2019**, *31* (29), 1901640. https://doi.org/10.1002/adma.201901640.

(31) Mohammed, A. K.; Usgaonkar, S.; Kanheerampockil, F.; Karak, S.; Halder, A.; Tharkar, M.; Addicoat, M.; Ajithkumar, T. G.; Banerjee, R. Connecting Microscopic Structures, Mesoscale Assemblies, and Macroscopic Architectures in 3D-Printed Hierarchical Porous Covalent Organic Framework Foams. *J. Am. Chem. Soc.* **2020**, *142* (18), 8252–8261. https://doi.org/10.1021/jacs.0c00555.

(32) Li, L.; Chen, R.; Li, Y.; Xiong, T.; Li, Y. Novel Cotton Fiber-Covalent Organic Framework Hybrid Monolith for Reversible Capture of Iodine. *Cellulose.* **2020**, *27* (10), 5879–5892. https://doi.org/10.1007/s10570-020-03189-4.

(33) Wang, Y.; Zhuo, S. Q.; Hou, J.; Li, W.; Ji, Y. Construction of β-Cyclodextrin Covalent Organic

Framework-Modified Chiral Stationary Phase for Chiral Separation. *ACS Appl. Mater. Interfaces.* **2019**, *11* (51), 48363–48369. https://doi.org/10.1021/acsami.9b16720.

(34) Liu, Z.; Wang, H.; Ou, J.; Chen, L.; Ye, M. Construction of Hierarchically Porous Monoliths from Covalent Organic Frameworks (COFs) and Their Application for Bisphenol A Removal. *J. Hazard. Mater.* **2018**, *355*, 145–153. https://doi.org/10.1016/j.jhazmat.2018.05.022.

(35) Li, C.; Yang, J.; Pachfule, P.; Li, S.; Ye, M.-Y.; Schmidt, J.; Thomas, A. Ultralight Covalent Organic Framework/Graphene Aerogels with Hierarchical Porosity. *Nat. Commun.* **2020**, *11* (4712). https://doi.org/10.1038/s41467-020-18427-3.

(36) Ding, L.-G.; Yao, B.-J.; Li, F.; Shi, S.-C.; Huang, N.; Yin, H.-B.; Guan, Q.; Dong, Y.-B. Ionic Liquid-Decorated COF and Its Covalent Composite Aerogel for Selective CO2 Adsorption and Catalytic Conversion. *J. Mater. Chem. A* **2019**, *7*, 4689–4698. https://doi.org/10.1039/c8ta12046c.

(37) Liu, X.; Yang, C.; Qian, H.-L.; Yan, X.-P. Three-Dimensional Nanoporous Covalent Organic Framework-Incorporated Monolithic Columns for High-Performance Liquid Chromatography. *ACS Appl. Nano Mater.* **2021**, *4* (5), 5437–5443. https://doi.org/10.1021/acsanm.1c00770.

(38) Wang, H.; Li, Z.; Feng, W.; Jia, Q. Polymer Monolith Containing an Embedded Covalent Organic Framework for the Effective Enrichment of Benzophenones. *New J. Chem.* **2017**, *41* (21), 13043–13050. https://doi.org/10.1039/c7nj02512b.

(39) Liu, X.; Lim, G. J. H.; Wang, Y.; Zhang, L.; Mullangi, D.; Wu, Y.; Zhao, D.; Ding, J.; Cheetham, A. K.; Wang, J. Binder-Free 3D Printing of Covalent Organic Framework (COF) Monoliths for CO2 Adsorption. *Chem. Eng. J.* **2021**, *403*, 126333. https://doi.org/10.1016/j.cej.2020.126333.

(40) Fan, C.; Wu, H.; Guan, J.; You, X.; Yang, C.; Wang, X.; Cao, L.; Shi, B.; Peng, Q.; Kong, Y.; Wu, Y.; Khan, N. A.; Jiang, Z. Scalable Fabrication of Crystalline COF Membrane from Amorphous Polymeric Membrane. *Angew. Chem. Int. Ed.* **2021**, anie.202102965.

https://doi.org/10.1002/anie.202102965.

(41) Haase, F.; Lotsch, B. V. Solving the COF Trilemma: Towards Crystalline, Stable and Functional Covalent Organic Frameworks. *Chem. Soc. Rev.* **2020**, *49*, 8469–8500. https://doi.org/10.1039/D0CS01027H.

(42) Smith, B. J.; Overholts, A. C.; Hwang, N.; Dichtel, W. R. Insight into the Crystallization of Amorphous Imine-Linked Polymer Networks to 2D Covalent Organic Frameworks. *Chem. Commun.* **2016**, *52*, 3690–3693. https://doi.org/10.1039/c5cc10221a.

(43) Liao, L.; Zhong, X.; Jia, X.; Liao, C.; Zhong, J.; Ding, S.; Chen, C.; Hong, S.; Luo, X. Supramolecular Organogels Fabricated with Dicarboxylic Acids and Primary Alkyl Amines: Controllable Self-Assembled Structures. *RSC Adv.* **2020**, *10*, 29129–29138. https://doi.org/10.1039/d0ra05072e.

(44) Feriante, C.; H., R.; Jhulki, S.; Evans, A. M.; Dasari, R. R.; Slicker, K.; Dichtel, W. R.; Marder, S. R. Rapid Synthesis of High Surface Area Imine-Linked 2D Covalent Organic Frameworks by Avoiding Pore Collapse During Isolation. *Adv. Mater.* **2020**, *32* (2), 1905776. https://doi.org/10.1002/adma.201905776.

(45) Krause, S.; Hosono, N.; Kitagawa, S. Chemistry of Soft Porous Crystals: Structural Dynamics and Gas Adsorption Properties. *Angew. Chem. Int. Ed.* **2020**, *59* (36), 15325–15341. https://doi.org/10.1002/anie.202004535.

(46) P¨utz, A. M.; Terban, M. W.; Bette, S.; Haase, F.; Dinnebier, R. E.; Lotsch, B. V. Total Scattering Reveals the Hidden Stacking Disorder in a 2D Covalent Organic Framework. *Chem. Sci.* **2020**, *11*, 12647–12654. https://doi.org/10.1039/d0sc03048a.

(47) Li, W.; Wu, W.; Li, Z.; Shi, J.; Xia, Y. Sol-Gel Asynchronous Crystallization of Ultra-Selective Metal-Organic Framework Membranes for Gas Separation. *J. Mater. Chem. A* **2018**, *6* (34), 16333–16340. https://doi.org/10.1039/c8ta06083e.

(48) Wang, J.; Wu, Y.; Cao, Y.; Li, G.; Liao, Y. Influence of Surface Roughness on Contact Angle Hysteresis and Spreading Work. *Coll. Polym. Sci.* **2020**, *298*, 1107 - 1112. https://doi.org/10.1007/s00396-020-04680-x/Published.

(49) Sick, T.; Rotter, J. M.; Reuter, S.; Kandambeth, S.; Bach, N. N.; Döblinger, M.; Merz, J.; Clark, T.; Marder, T. B.; Bein, T.; Medina, D. D. Switching on and off Interlayer Correlations and Porosity in 2D Covalent Organic Frameworks. *J. Am. Chem. Soc.* **2019**, *141* (32), 12570–12581. https://doi.org/10.1021/jacs.9b02800.

(50) Chen, R.; Hu, T.; Li, Y. Stable Nitrogen-Containing Covalent Organic Framework as Porous Adsorbent for Effective Iodine Capture from Water. *React. Funct. Polym.* **2021**, *159*, 104806. https://doi.org/10.1016/j.reactfunctpolym.2020.104806.

(51) Uribe-Romo, F. J.; Doonan, C. J.; Furukawa, H.; Oisaki, K.; Yaghi, O. M. Crystalline Covalent Organic Frameworks with Hydrazone Linkages-Tris(4-Formylphenyl)Benzene (Blue) to Form COF-42 and COF-43 (Cavity Sizes Are Indicated). *J. Am. Chem. Soc* **2011**, *133*, 55. https://doi.org/10.1021/ja204728y.

For Table of Contents (TOC) use only